Article

Predicting the Sauter Mean Diameter of Swirl Cup Airblast Fuel Injector Based on Backpropagation (BP) Neural Network Model

Chuanyu Fang, Fuqiang Liu, Jinhu Yang, Shaolin Wang,* Cunxi Liu,* Yong Mu, Gang Xu, Junqiang Zhu, and Yushuai Liu
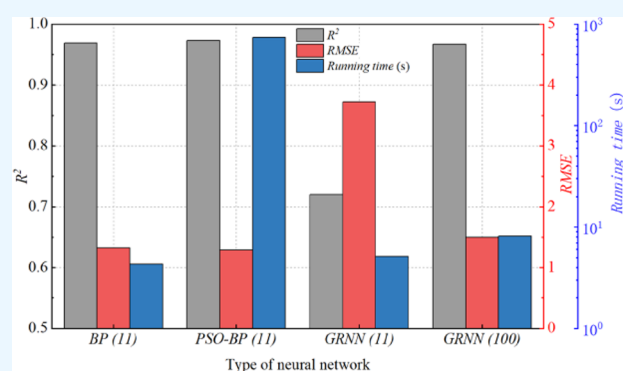
Read Online

ACCESS | Metrics & More | Article Recommendations

ABSTRACT: This study was dedicated to introducing a new method for predicting the Sauter mean diameter (SMD) buildup in the swirl cup airblast fuel injector. There have been considerable difficulties with predicting SMD mainly because of complicated flow characteristics in a spray. Therefore, the backpropagation (BP) neural network-based machine learning was applied for the prediction of SMD as a function of geometry, condition parameters, and axial distance such as primary swirl number, secondary swirl number, venturi angle, mass flow rate of fuel, and relative air pressure. SMD was measured by a phase Doppler particle analyzer (PDPA). The results show that the prediction accuracy of the trained BP neural network was excellent with a coefficient of determination (R^2) score of 0.9599, root mean square error (RMSE) score of 1.4613, and overall relative error within 20%. Through sensitivity analysis, the relative air pressure drop and primary swirl number were the largest and smallest factors affecting the value of SMD, respectively. Finally, the prediction accuracy of the BP neural network model is far greater than the current prediction correlations. Moreover, for the predicting target in the present study, the BP neural network shows the advantages of a simple structure and short running time compared with PSO-BP and GRNN. All these prove that the BP neural network is a novel and effective way to predict the SMD of droplets generated by a swirl cup airblast fuel injector.

1. INTRODUCTION

Swirl cup airblast fuel injector has excellent fuel atomization performance, uniform fuel−air mixing, and remarkable emission reduction ability and it is widely used in modern-day gas turbine combustors.[1] Over the past few decades, it has received extensive attention for its excellent performance. Many researchers have focused their studies on the flow field, spray characteristics, and combustion performance of a swirl cup airblast fuel injector. Fu et al.[2] studied the effects of confinement venturi type on the flow field of a turbulent confined swirling flow and concluded that the size and strength of the recirculation zone were highly affected by the level of confinement. Lin et al.[3] studied the effect of the geometric modification of the venturi on the no-reacting flow, they found that the venturi significantly influenced the interactions of the swirling motions between the primary and secondary flows. Liu et al.[4] studied the swirl angle on the spray performance, they found that a big swirler angle contributed to the mixing of air and fuel and eventually improved the ignition and lean blow-out (LBO) combustion performances. Wang et al.[5] studied the hardware design of the flow field structure and found that the flare influenced the size of the recirculation zone and droplet dispersion. Becker and Hassa[6] and Shanmugadas et al.[7] studied

the fuel placement and droplet size inside the swirl cup using PDI and PLIF. They highlighted that swirl shear layers should be considered in fuel injector designs for improving atomization and interactions between fuel and the air shear layer. Ying et al.[8] reviewed the dynamics and stability of swirl cup combustor and flow characteristics influencing the atomization processes such as vortex breakdown, processing vortex core (PVC), central toroidal recirculation zone (CTRZ), etc. Im et al.[9] conducted an experimental study on the influence of structural parameters of the venturi on atomization. They found that the longer the venturi tube is, the larger the spray cone angle is and the smaller the droplets generated. Moreover, the venturi with a throat will make the droplet size distribution more uniform. Ateshkadi et al.[10] studied the effect of venturi on atomization and fuel distribution by using the PLIF technique. The results showed that the structure of the venturi

has a great influence on the breakup process of liquid film and the downstream distribution of droplets. In addition, the venturi limited the spray to a smaller region compared with the case without the venturi. Liu et al.[11] investigated the spray characteristics that influence the flame pattern and combustion stability. Their results highlight that spray quality affects combustion stability at ignition and close to LBO.

It can be seen from previous studies that atomization, as the first stage of combustion, will directly affect combustion efficiency and combustion stability. Thus, for engineering design, it is quite useful to provide some estimates on the performances of swirl cup airblast fuel injectors under various conditions. The Sauter mean diameter (SMD) is widely accepted as an average droplet size parameter in combustion applications that controls the evaporation rate, which is defined as follows

$$\text{SMD} = \frac{\sum nD^3}{\sum nD^2} \tag{1}$$

Lefebvre et al.[12] concluded that smaller SMD promoted fuel evaporation and decreased the demand for ignition energy. Hashimoto et al.[13] found that SMD directly determined the soot formation characteristics in the flame. The critical factors that influence the spray are airflow velocity, fluid viscosity, surface tension, and density.

A large number of studies have been carried out on the influencing factors of the SMD of spray generated by a swirl cup fuel injector. Many studies have proposed empirical and semiempirical SMD correlations. Lefevre et al.,[1] Jasuja et al.,[14] Urbán et al.,[15] Chong et al.,[16] Shanmugadas et al.,[7] and others have done a lot of meaningful work on the effects of atomizer scale, alternative fuels, impingement angle of air onto a liquid sheet, and classical and prompt atomization on SMD, and proposed many widely used SMD empirical correlations, However, current SMD correlations mainly focused on liquid properties, particularly viscosity. The influence of geometric changes was not validated systematically and the application range of prediction was limited.

Backpropagation (BP) neural network has the advantages of self-adaption, self-learning, nonlinear mapping, and fault tolerance, which can fit more complicated causal relationships and has been successfully applied to prediction in many fields.[17] Nowadays, the BP neural network is widely used in industry, agriculture, food, construction, etc. Cui et al.[18] proposed the prediction model of multicomponent surrogates based on the BP neural network to predict ignition delay. The results showed that the neural network model was able to realize high accuracy of octane number (RON) and motor octane number (MON) with a maximum deviance of no more than three units. Zhao et al.[19] used a bidirectional recurrent neural network (bi-RNN) to predict flow fields inside an engine cylinder at different time steps by particle image velocimetry (PIV). According to the results, during the early intake stroke and compression stroke, the global indices could reach 0.9. Kaiser et al.[20] applied the machine learning algorithm based on an artificial neural network to closed coupled atomization nozzle research. The predicted results obtained a high $R^2 = 0.98$ at most positions, which was in good agreement with the experimental results. Park et al.[21] used an optimized ANN to predict the operating characteristics of the combustion chamber and conducted a sensitivity analysis by using the real-time data of the industrial gas turbine. The

turbine exhaust temperature and the main design parameters of the gas turbine were used as input parameters to predict the fuel flow, turbine inlet temperature, fuel distribution of each nozzle, NOx, working pressure of the combustion chamber, and inlet air temperature. The result of the sensitivity analysis of input parameters showed that the influence of ambient conditions is very small.

However, only a limited number of researchers have conducted SMD prediction in neural networks using a fuel nozzle. Taghavifar et al.[22] used the artificial neural network-genetic algorithm(ANN-GA) to predict spray liquid tip penetration and SMD in a diesel engine. Consequently, $R^2 = 0.994$ for penetration, whereas SMD yields a lower amount of 0.992. Kaveh et al.[23] used the general regression neural network (GRNN) to predict the velocity and SMD in liquid−liquid coaxial swirl injectors. The general regression neural network had a good performance, achieving a velocity prediction accuracy of 93%. Liu et al.[24] constructed GA-BP for supersonic atomized water to predict the SMD. The results are consistent with the experimental results. The prediction by GA-BP is better with $R^2 = 0.979$.

According to previous research, the majority of studies on SMD prediction in fuel nozzles have relied on traditional semiempirical correlations, and the application range of prediction was limited. Only a few researchers have explored the use of complex machine learning models for SMD prediction. In addition, to the best of our knowledge, swirler cup airblast injectors have not been used to establish a machine learning model for SMD prediction. Moreover, the relative influence weights of geometry and fuel/air supply condition parameters affecting the SMD are not clear. The main aim of this study is to develop SMD correlations based on the BP neural network. To achieve this goal, the BP neural network was trained and further validated with an extra data set in order to predict SMD of spray generated by swirl cup airblast fuel injector with high accuracy and wide application range under different geometry and condition parameters. Then, sensitivity analysis was also conducted to extract the most significant parameters affecting the SMD. Further, we compared the final trained BP neural network with the current SMD correlations and other neural networks to verify the performance of the BP neural network.

2. EXPERIMENTAL APPARATUS AND METHODOLOGY

2.1. Swirl Cup Fuel Injector. Figure 1 schematically shows the swirl cup airblast fuel injector used in this study. The pressure-swirl atomizer is located at the center of the swirl cup, which generates an 80° hollow cone spray. Eight elliptical tangential primary jets are used to generate the primary
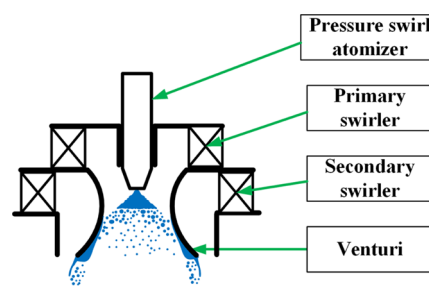

Figure 1. Detailed information on the swirl cup airblast fuel injector.

swirling stream, and a radial secondary swirler has 10 blocks to introduce the co- or counter-rotating air streams into the swirl cup. During the swirl cup working process, most droplets generated by the pressure-swirl atomizer impinge on the venturi and form a thin liquid film on the venturi's inner surface. At the edge of the venturi, the thin liquid sheet undergoes intense shearing action by co- or counter-rotating air streams and breaks up into ligaments. Meanwhile, the stronger secondary swirling airflow undergoes vortex breakdown, creating a central toroidal recirculation zone (CTRZ) at the swirl cup exit. Very few droplets from the pressure-swirl atomizer directly flow out of the swirl cup without impingements on the venturi. The geometric parameters of the swirl cup in this study are given in Table 1.

Table 1. Variation Range of Geometric Parameters Investigated

test case	SN_p	SN_s	θ_v
base	−1.090	0.443	50
Case 1	−0.803	0.443	50
Case 2	−1.557	0.443	50
Case 3	1.334	0.443	50
Case 4	1.557	0.443	50
Case 5	−1.090	0.770	50
Case 6	−1.090	0.291	50
Case 7	−1.090	0.443	30
Case 8	−1.090	0.443	70

Swirl number (SN) quantifies the relative strength of swirl produced by the swirler, which is varied by primary and secondary swirler angles in this study and it was originally proposed by Beer[25]

$$SN = \frac{G_\varphi}{G_z R} \tag{2}$$

where G_φ is the axial flux of the angular momentum, G_z is the axial thrust, and R is the exit radius of the swirler.

The primary swirl number can be derived based on eq 2

$$SN_p = \pm \frac{R_e R_v}{kwd} \sin \alpha \tag{3}$$

where R_e is the radius of the primary swirler exit, R_v is the radius of the venturi exit, k is the number of vanes in the cascade, wd is the axial width of a channel, and α is the primary swirler angle. In this study, the flow direction is changed to co-rotation or counter-rotation by altering the blade direction in the primary swirler and keeping the secondary swirler constant. For example, the blade direction in a primary swirler is clockwise, while that in a secondary swirler is oriented in a counterclockwise manner to yield a counter-rotation swirl flow and vice versa for co-rotation.

The following equation was used to find the swirl number of the secondary swirler.[26]

$$SN_s = 0.28 \frac{1}{1 - \psi} \frac{\tan \beta}{1 + \tan \beta \tan\left(\frac{\pi}{n}\right)} \tag{4}$$

where n is the number of blades, ψ is the blockage factor, and β is the secondary swirler angle.

ψ can be written as

$$\psi = \frac{ns}{2\pi R_s \cos \beta} \tag{5}$$

where s is the thickness of the vanes and R_s is the radius of the secondary swirler exit.

2.2. Experimental Setup and Diagnostic Techniques. The atomization test rig is illustrated in Figure 2, which
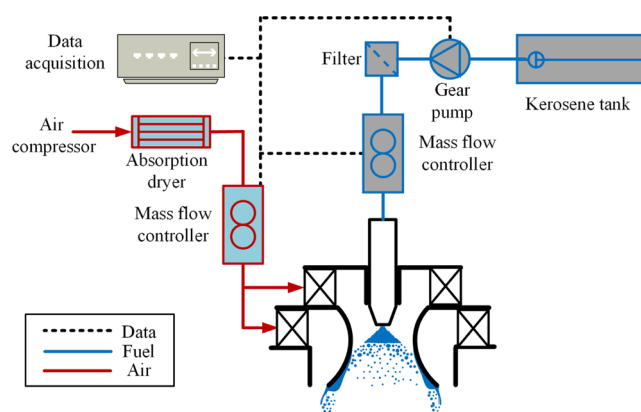

Figure 2. Experimental setup.

consists of three major components: air/fuel supply and control system, optical devices PDPA, and swirl cup airblast fuel injector. LabVIEW-based program and NI-CDAQ-9186 board were used to control the air/fuel supply system. Air was supplied by a compressor. Before entering the swirl cup, the air was dried by an adsorption dryer and stored in a surge tank. The tank was connected to the swirl cup airblast fuel injector through the air mass flow controller (0−300 lpm, ±2%). The PSI pressure difference sensors (0−10 psi, ±0.05%) were arranged before and after the swirl cup to measure the inlet total air pressure and outlet static pressure. The relative air pressure drop $(\Delta P_a/P_a)$ across the swirler was defined as the difference between total pressure at the inlet and at the outlet divided by the total pressure at the inlet. The fuel tank was connected to the swirl cup airblast fuel injector through a gear pump, oil filter, ball valve, and fuel mass flow controller (0−20 kg/h, ±0.1%). A pressure transducer (0−0.6 MPa, ±0.1%) was used to record the fuel pressure. Relative air pressure drop and fuel mass flow rate were adjusted by controlling the fuel mass flow controller and gear pump output power. To reduce the error of measurement, every instrument was zero-calibrated before tests.

Phase Doppler particle analyzer (PDPA) was used to measure the droplet size, which was installed on a computer-controlled three-axis traverse system (moving range 600 × 600 × 600 mm³, accuracy 0.01 mm). An argon ion laser was used to supply a continuous wave with a 514.5 nm wavelength. The integrated transmitter unit divided the laser beam into two beams with a 40 MHz frequency shift. The incident laser beams were scattered from a 500 mm focal length transmitting optic. A receiving optic with a 750 mm focal length was also positioned in the forward scattering direction. The laser emitted by the transmitting optics was scattered by droplets and then entered the receiving optics. Subsequently, the received optical signal was transferred to the PDPA processor to convert it into an electrical signal and sent to the computer. The PDPA details are shown in Table 2.

2.3. Test Conditions. The fuel used was BP-3 kerosene, whose physicochemical properties were similar to those of Jet

Table 2. PDPA Setting Parameters

parameter	value
laser	argon ion laser 3W
wavelength	514.5 nm
beam waist	126.64 μm
beam separation	50 mm
Bragg frequency	40 MHz
front focal length of transmitting and receiving optics	500 mm, 750 mm
scattering angle	33°
receiving optics	refraction
polarization	perpendicular

A-1. The detailed fuel properties can be found in a study by Ma[27] et al. The test was carried out at room temperature and pressure with four different relative air pressure drops ($\Delta P_a/P_a$ 2%, 3%, 4%, 5%) and five mass flow rates of fuel (m_f 2.0, 2.5, 3.0, 3.5, 4.0 kg/h). Thus, the number of operating conditions for each type of swirler cup was 20.

The PDPA measurements were carried out at five axial positions (Z = 20, 30, 40, 50, 60 mm), and at each axial location, radial measurements were carried out with an interval of 2 mm until the spray edge. The measured SMD values at several radial locations for each axial position were used to calculate a single value of the line-of-sight SMD. The line-of-sight SMD was the averaged SMD over each axial location and weighted by the measured volume flux at each radial location. Therefore, the line-of-sight SMD used in this study was defined as[28]

$$\text{SMD} = \frac{\sum_{r=R}^{r=1} \text{SMD}_r \times n_r}{\sum n_r} \quad (6)$$

where n_r was the valid volume flux of droplets in the axial direction through the probe volume at every measured point and r was the radial distance of measurement points from the swirler cup axis.

2.4. BP Neural Network. *2.4.1. Basic Construction of BP Neural Network.* An artificial neural network (ANN) is an adaptive system that mimics the biological neural network of the human brain.[29] As a classic algorithm in ANN, a backpropagation (BP) neural network was widely used to establish predictive models because of its abilities of self-learning, arbitrary function approximation, and seeking solutions at a high speed.[30] Depending on their task, the BP neural network is divided into three different layers: input, hidden, and output. In this study, the relative air pressure drop ($\Delta P_a/P_a$), fuel mass flow rate (m_f), primary swirl number (SN_p), secondary swirl number (SN_s), venturi angle (θ_v), and axial location (Z) are selected as input parameters, and SMD is selected as output parameters. The structure of the BP neural network is shown in Figure 3.

Each neuron in the network was fully connected to each other in the next layer. When the input data were introduced to the neurons in the input layer, they were multiplied by weights connecting them to the neurons in the hidden layer; the weighted input data were then summed and reached the hidden layer after the nonlinear conversion of the activation function. The hidden data finally entered the output layer of the neuron after the same steps. This process was continued in the forward layer by layer. The functional relationship represented by the network structure can be expressed as follows
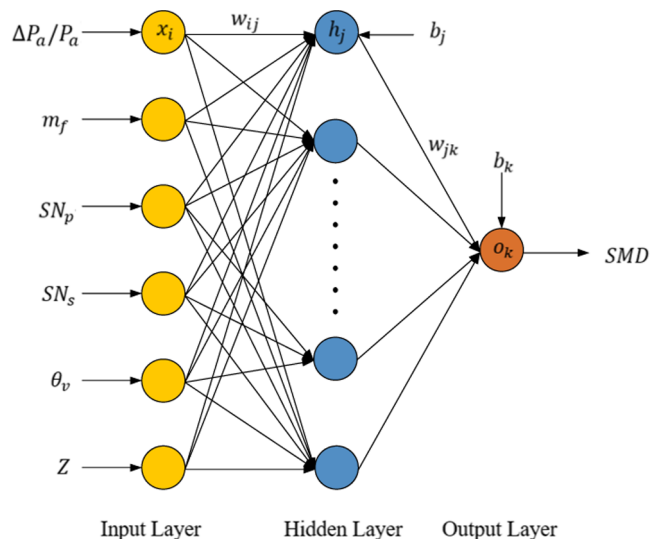

Figure 3. Diagram of BP neural network.

$$\text{SMD} = \varphi\left(\sum_{j=1}^{5} f\left(\sum_{i=1}^{6} w_{ij}x_i + b_j\right) + b_k\right) \quad (7)$$

where x_i is the input layer neuron (i = 1−6), h_j is the hidden layer neuron (j = 1−5), o_k is the output layer neuron (k = 1), w_{ij} is the weight of the connection between the input layer neurons and the hidden layer neurons, and b_j is the bias for the hidden layer neuron. Similarly, w_{jk} is the weight of the connection between the hidden layer neurons and the output layer neurons and o_k is the bias for the output layer neuron. $f(.)$ and $\varphi(.)$ represent the activation functions of the hidden layer and output layer, respectively. In this study, the Tansig function was used as the hidden layer activation function $f(.)$, and the Pureline function was used as the output layer activation function $\varphi(.)$, which are defined as follows

$$\text{tansig}(x) = \frac{e^x - e^{-x}}{e^x + e^{-x}} \quad (8)$$

$$\text{pureline}(x) = x \quad (9)$$

The training process aimed to minimize the error function defined as the difference between the predicted output and the desired output. Randomly setting the initial weight and bias, the Levenberg−Marquardt (LM) backpropagation algorithm was run to calculate the error. If the error was bigger than a certain threshold, the weights and bias iteratively updated in a gradient-descent direction of the error. This process was repeated until the error was reduced to an acceptable level.[31]

Since the final weights and bias performing best for the target database are not necessarily applicable to other databases, the trained BP neural network needed two additional steps to crosscheck, namely, validation and test steps,[32] and the number of training data sets needed to be large enough to avoid overfitting.[33]

In this study, an error backpropagation algorithm was developed to establish the BP neural network model. A total of 900 sets of data were trained to avoid overfitting. The data were randomly divided into a training set, validation set, and test set. Each trained neural network was different, so it needed to be trained multiple times to get the minimum error.

2.4.2. Data Preparation and the Number of Neurons in the Hidden Layer. In this study, 900 samples were collected from the experiments and randomly divided into three groups, namely, 80% of the data for training, 10% for validation, and 10% for testing of the BP neural network model. In order to improve the training efficiency and avoid the largest input parameters being overwhelmed by the influence of other parameters, which reduced the prediction accuracy, all data must be normalized to the standardized data between 0 and 1 so that the parameters with large differences in the original distribution have the same weight effect on the model. The calculation formula is presented in eq 10

$$x_{st} = \frac{(x - \overline{x})}{SD} \tag{10}$$

where x is the original data, x_{st} is the normalized data, $\overline{x}$ is the mean value of data, and SD is the standard deviation.

According to previous research results,[34] unless the data used for the BP neural network were of peculiar discontinuity, a hidden layer was sufficient to approximate most functions. Therefore, a hidden layer of the BP neural network was used in this study.

After determining the number of hidden layers, a key step was to select the appropriate number of hidden layer neurons, which was set according to the empirical equation 11.[35]

$$N = \sqrt{I + O} + h \tag{11}$$

where N is the number of neurons in the hidden layer, I is the number of neurons in the input layer, O is the number of neurons in the output layer, and h represents the constant between 1 and 10.

According to eq 11, the number of hidden layer neurons was 3−12. A trial-and-error method determined the number of hidden layer neurons. Different numbers of neurons were used for training, and the quality of the neural network was determined by comparing the root mean square error (RMSE) and the coefficient of determination (R^2). RMSE is the mean square error between the output and target, which is usually used to evaluate the similarity between the predicted value and the actual value. The lower RMSE indicates a better robustness of the model. The R^2 value was usually used to measure the correlation between the predicted value and the target value. The R^2 value close to 1 means that there is a close relationship between the predicted results and the actual data, indicating that the prediction accuracy was high. RMSE and R^2 can be calculated as follows in eq 12

$$R^2 = 1 - \frac{\sum_{i=1}^{n} (y_i^M - y_i^P)^2}{\sum_{i=1}^{n} (y_i^M - \overline{y})^2} \tag{12}$$

$$RMSE = \sqrt{\frac{1}{n} \sum_{i=1}^{n} (y_i^M - y_i^P)^2} \tag{13}$$

where y^M is the measured value of SMD, $\overline{y}$ is the mean value of y^M, and y^P is the predicted value of SMD with a BP neural network.

As shown in Figure 4 with the increase in the number of neurons, RMSE gradually decreased and R^2 gradually increased. When the number of hidden layer neurons was 11, the maximum R^2 and minimum RMSE were obtained, indicating that the BP neural network with 11 neurons in the
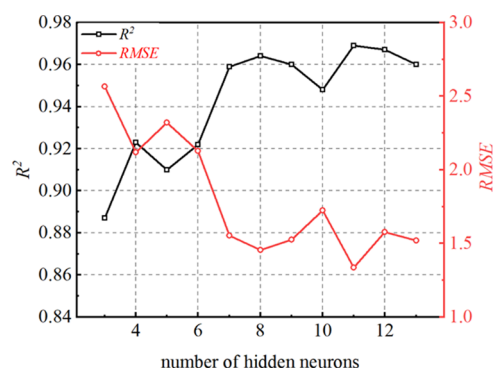

Figure 4. Variation of RMSE and R^2 with the number of hidden neurons.

hidden layer performed best according to the RMSE and R^2 results.

In addition, the trial-and-error method was also used to check whether the data set size was appropriate. As shown in Figure 5, with the increase in the size of the data set, RMSE
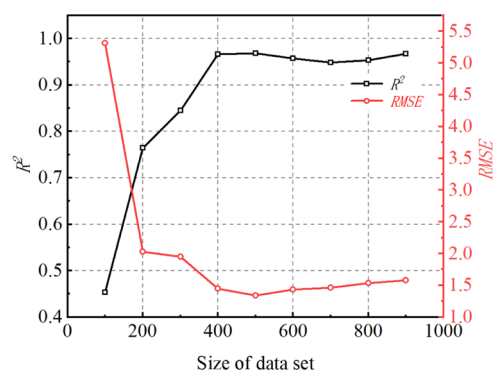

Figure 5. Variation of RMSE and R^2 with the size of the data set.

gradually decreased and R^2 gradually increased until the size of the data set reached 400. This indicated that a 900 data set is enough for training the BP network used in the present study.

3. RESULTS AND DISCUSSION

3.1. BP Neural Network Training Results and Experimental Validation. Figures 6−9 show the regression plot of final results, training, validation, testing, and the overall process in this study. As illuminated in Figure 6−9, the black
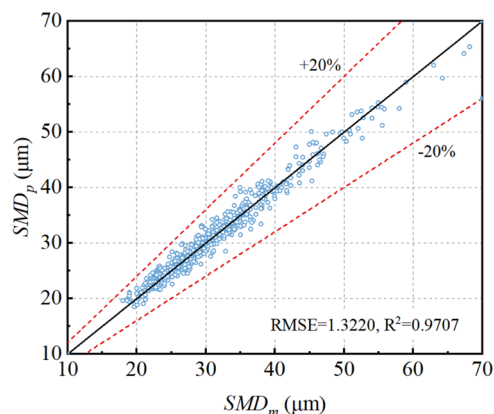

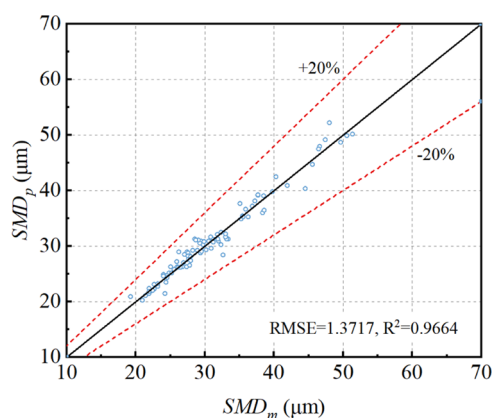**Figure 6.** Regression analysis for the training step.

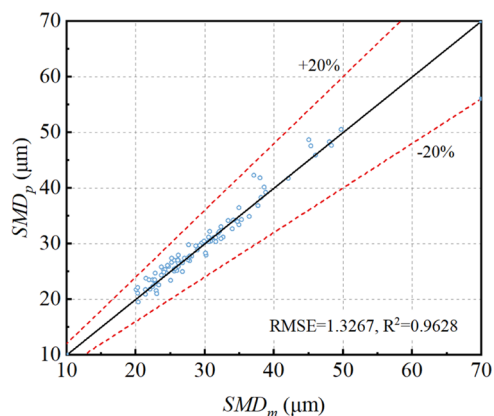**Figure 7.** Regression analysis for the validation step.

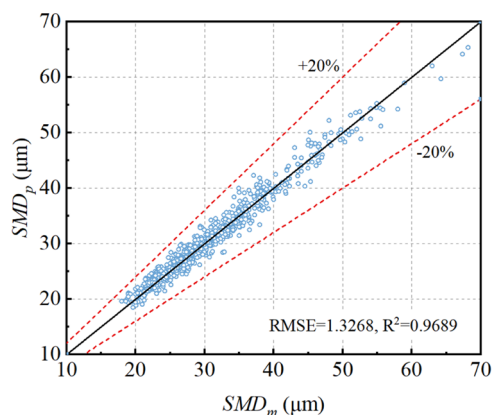**Figure 8.** Regression analysis for the test step.

Figure 9. Regression analysis for the BP neural network.

solid line indicated that the predicted value was equal to the actual value, namely, the most optimal prediction result; the relative error (RE) was defined to represent the prediction accuracy of a single point, which can be calculated as

$$\mathrm{RE} = \frac{y^{\mathrm{M}} - \overline{y}}{\overline{y}} \times 100\% \tag{14}$$

The closer the predicted points were to the black solid line, the smaller the relative error of the prediction results was. All of the relative errors between the predicted value of SMD and the experimental data were less than 20%, indicating that the prediction results of the BP neural network are very

satisfactory, independent of the randomly grouped training, validation, and testing data. It was also worth noting that in these three processes, R^2 was higher than 0.96, indicating that the prediction accuracy was high.

To further validate the BP neural network training results and avoid the phenomenon of overfitting, an extra set of experimental data was selected for testing. The geometry and condition parameters are shown in Table 3. This set of data

Table 3. Geometry and Condition Parameters for Extra SMD Tests

specification	value
relative air pressure drop, $\Delta P_a/P_a$ (%)	2−5
fuel mass flow rate, m_f (kg/h)	2.0−4.0
primary swirl number, SN_p	−0.803
secondary swirl number, SN_s	0.770
venturi angle, θ_v (deg)	50
axial location, Z (mm)	20−50

was not used in the previous process (training, validation, and test). The prediction results of the BP neural network are shown in Figure 10. The RMSE and R^2 values were 1.4613 and
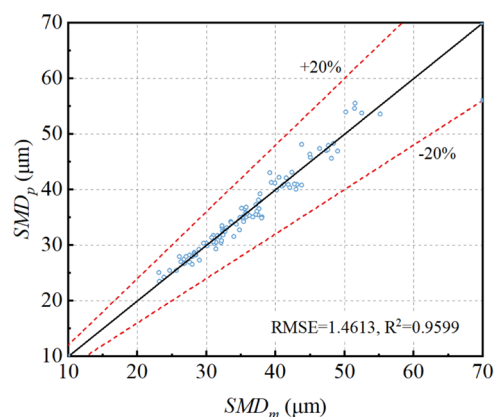

Figure 10. Regression analysis for the extra set of experimental data.

0.9599, respectively. The relative error of the predicted SMD for the whole extra data set is less than 20%, and 90% of the data point error is less than 10%, indicating that the model did not show overfitting problems and had a wide range of applications. Hence, the BP neural network was able to predict the SMD of droplets generated by a swirl cup airblast fuel injector with other geometries and condition parameters.

In order to further analyze the prediction accuracy, Figures 11−15 show the measured and predicted values of SMD for the change of $\Delta P_a/P_a$ and m_f with different Z in extra SMD tests. Solid lines represent BP neural network prediction results, and discrete points represent experimental results. With the increase of m_f both measured and predicted SMD values show a declination tendency, this was because the fuel supply pressure also increased with the increase of m_f, which improved the atomization quality of the pressure fuel injector.

A comparison of the predicted and measured values showed that the predicted SMD results were larger regardless of the $\Delta P_a/P_a$ and m_f at Z = 20 and 30 mm, and SMD differences of up to 3.94 μm were observed at Z = 20 mm, m_f = 3 kg/h, and $\Delta P_a/P_a$ = 2%. In addition, most of the predicted values were large relative to the actual values at Z = 40−60 mm, and the
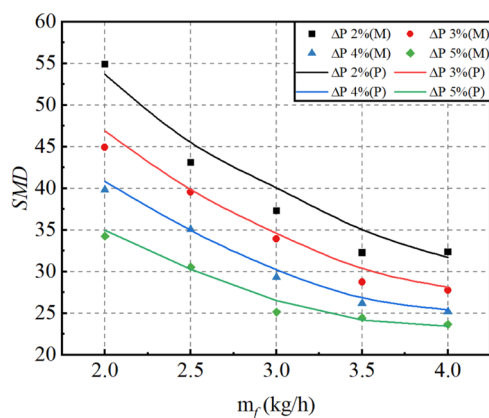
Figure 11. Comparison between predicted and measured values of SMD at $Z = 20$ mm.
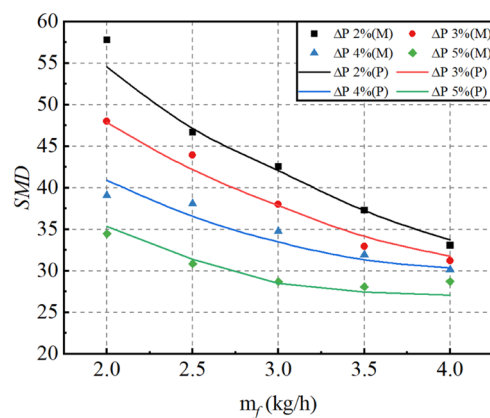

Figure 12. Comparison between predicted and measured values of the SMD at $Z = 30$ mm.

Figure 13. Comparison between predicted and measured values of SMD at $Z = 40$ mm.

Figure 14. Comparison between predicted and measured values of SMD at $Z = 50$ mm.
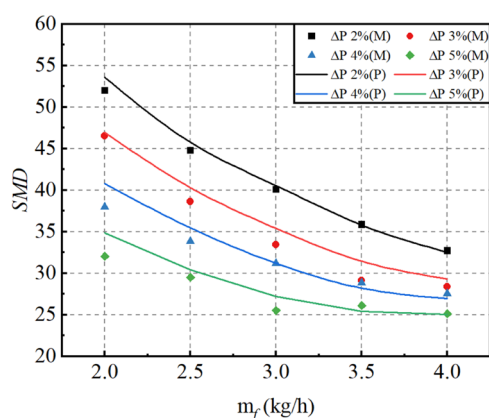

Figure 15. Comparison between predicted and measured values of SMD at $Z = 60$ mm.
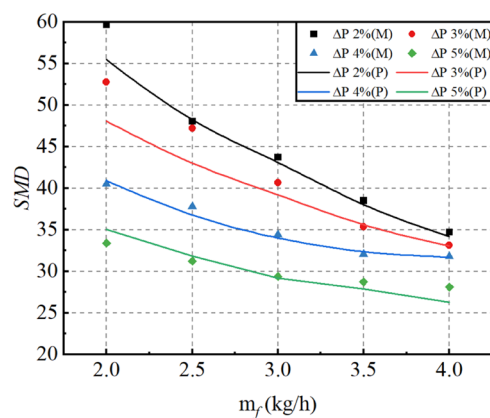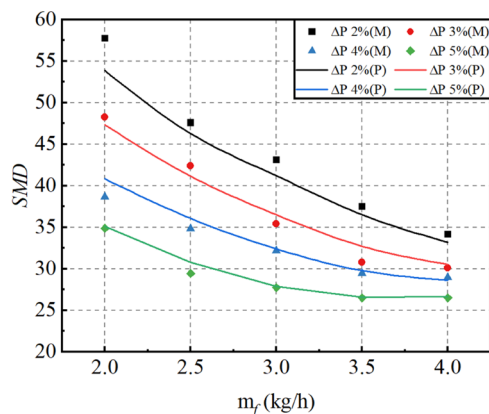
maximum difference of 2.52 μm is observed at $Z = 60$ mm, m_f = 32 kg/h, and $\Delta P_a/P_a = 2\%$. This indicated that the prediction accuracy of the neural network was better at $Z = 40-60$ mm. The reason was that the data used in the training step came from different geometries, and the different geometries born about the change of the near swirler flow field further affected atomization. At $Z = 20$ and 30 mm, the spray was not completely secondary atomized; as a result, the particle size fluctuated greatly, which had an adverse effect on the prediction accuracy of the neural network. However, at $Z =$ 40−60 mm, the spray was completely atomized under different geometries, and the variation of spray particle size was relatively slight, which was beneficial to the prediction of the neural network.

3.2. Sensitivity Analysis. Although the trained neural network can predict the SMD values well, it can be difficult to obtain a clear physical or functional relationship between the SMD values predicted by the BP neural network and the input parameters.

Therefore, a systematic "elimination method" sensitivity analysis was conducted to analyze the influence of the initial input parameters on the prediction accuracy and to determine the most significant parameter.[36]

In the first step, every parameter among the six parameters was eliminated, and other parameters were retained. Then, the process was performed on the remaining parameters to obtain a new BP neural network model, and the new model was compared with the original model trained with all input parameters in terms of both R^2 and RMSE. If the eliminated parameter was critical for SMD, the new model trained by eliminating this parameter would have higher RMSE and lower R^2.

The results of the sensitivity analysis are illustrated in Table 4 and Figure 16, which compared the R^2 and RMSE with the results after eliminating $\Delta P_a/P_a$, m_f, SN_p, SN_s, θ_v, and Z, respectively.

The results show that the trained neural network has the highest R^2 and the lowest RMSE after eliminating the input

Table 4. Sensitivity Analysis Results for Input Parameters

case	eliminated input parameter	R^2	RMSE
Case 1	NA	0.9689	0.0443
Case 2	m_f	0.5272	0.1381
Case 3	$\Delta P_a/P_a$	0.4437	0.1831
Case 4	SN_p	0.8548	0.0840
Case 5	SN_s	0.7824	0.0976
Case 6	θ_v	0.7664	0.0936
Case 7	Z	0.7747	0.1086
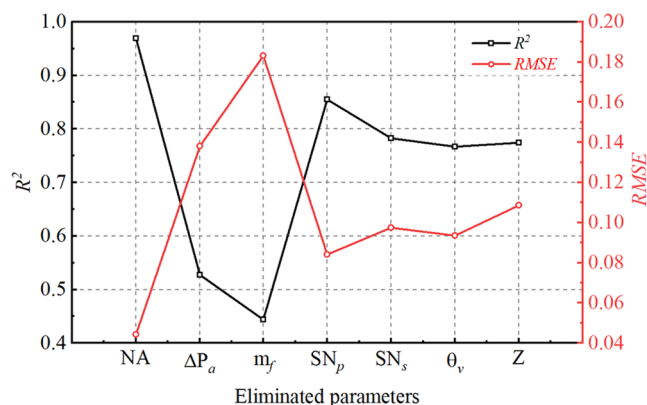
Figure 16. Sensitivity analysis results for the input parameter.

parameter of SN_p, which indicated that SN_p had the least effect on the prediction accuracy of SMD. After eliminating the $\Delta P_a/P_a$, the trained neural network had the smallest R^2 and the highest RMSE, indicating that the $\Delta P_a/P_a$ was the main factor that affected the prediction accuracy of SMD.

From the results, we can also determine that the R^2 and RMSE of the trained neural network vary greatly by excluding m_f and $\Delta P_a/P_a$, which are the two condition parameters, respectively, while the R^2 and RMSE of the trained neural network vary little by excluding the number of SN_p, SN_s, and θ_v, which were the three geometrical parameters, indicating that for the nozzle used in this study, the effect of condition parameters was greater than that of the geometry parameters.

3.3. Comparison between BP Neural Network and SMD Correlation Formulas. As mentioned in the Introduction section, a large number of studies have been conducted on airblast atomization in the past few decades and presented many empirical and semiempirical correlation formulas for estimating SMD. These correlations connect SMD with the operating range of air and the liquid, measurement location, and the type of injector. To evaluate the BP neural network, it is necessary to compare the prediction accuracy of the BP neural network and SMD correlations.

The BP neural network performances based on SMD results at 50 mm downstream of the swirl cup exit for samples in Table 3 are compared with that of the existing correlations, which are listed in Table 5.

Table 5. Correlations to Predict SMD from Previous Investigations

number	SMD correlations	
(15)	$$\text{SMD}/d_0 = A\left(\frac{\sigma}{u_a^2 \rho_a}\right)^{0.5}(1 + 1/\text{ALR}) + B\left(\frac{\mu_f^2}{\sigma \rho_f}\right)^{0.5}(1 + 1/\text{ALR}) \quad (15)$$	Lefebvre[1]
(16)	$$\text{SMD} = A\left(\frac{\sigma}{u_a^2 \rho_a}\right)^{0.45}(1 + 1/\text{ALR})^{0.5} + B\left(\frac{\mu_f^2}{\sigma \rho_f}\right)^{0.4}(1 + 1/\text{ALR})^{0.8} \quad (16)$$	Jasuja[14]
(17)	$$\text{SMD} = Cd_0\left(\frac{\sigma}{u_a^2 \rho_a}\right)^{0.5}(1 + 1/\text{ALR}) \quad (17)$$	Urbán[15]
(18)	$$\text{SMD} = A\left(\frac{(\sigma \mu_f)^{0.33}}{\rho_f^{0.37} \rho_a^{0.3} u_a}\right)(1 + 1/\text{ALR})^{1.7} + B\left(\frac{\mu_f^2 d_0}{\sigma \rho_f}\right)^{0.5}(1 + 1/\text{ALR})^{1.7} \quad (18)$$	Chong and Hochgreb[16]
(19)	$$\text{SMD} = A\frac{\sigma}{\rho_f u_f}^{0.6}\left(\frac{\rho_f}{\rho_a}\right)^{0.1} d_0^{0.4}(1 + 1/\text{ALR}) + B\frac{\mu_f^2 d_0}{\sigma \rho_f}^{0.5}(1 + 1/\text{ALR}) \quad (19)$$	Shanawany and Lefebvre[37]
(20)	$$\text{SMD}/d_0 = A\left(\frac{\sigma}{u_a^2 \rho_a}\right)^{-0.4}(1 + 1/\text{ALR})^{0.4} + B\left(\frac{\mu_f^2}{\sigma \rho_f}\right)^{0.5}(1 + 1/\text{ALR}) \quad (20)$$	Rizk and Lefebvre[38]
(21)	$$\text{SMD} = C\left(\frac{\rho_f}{\rho_a}\right)^{0.25}\left(\frac{\mu_f}{\rho_f u_a d_0}\right)^{0.5}\left(\frac{\sigma}{u_a^2 \rho_a}\right)^2 \quad (21)$$	Hsiang and Faeth[39]
(22)	$$\text{SMD} = C\frac{\sigma^{0.75}}{u_a^{1.57}} \quad (22)$$	Sattelmayer and Wittig[40]
(23)	$$\text{SMD} \propto \sigma^{0.5} \rho_a^{-0.4} u_a^{-1.05} \mu_f^{0.15}\left(\frac{m_f}{\rho_f}\right)^{0.15} \delta^{0.3} \quad (23)$$	Aigner and Wittig[41]
(24)	$$\text{SMD} = C\mu_f^{0.633} P_f^{-0.507} P_a^{-4.565e-3} \quad (24)$$	Chen[42]
(25)	$$\text{SMD} = \frac{C(\rho_f \mu_f)^{0.25} \sigma^{0.5}}{\rho_a^{0.75}[u_a(1 + \sqrt{\rho_a/\rho_f}) - u_f]u_a^{0.25}} \quad (25)$$	Varga[43]

Table 6. Comparison of Prediction Accuracy between Prediction Correlations and BP Neural Network at Z = 50 mm

| ΔP_{air}	m_{fuel}	(15)	(16)	(17)	(18)	(19)	(20)	(21)	(22)	(23)	(24)	(25)	(BP)
2%	2.0kg/h	7%	9%	-25%	7%	-5%	13%	-26%	-26%	16%	14%	-23%	2%
	2.5kg/h	-5%	-4%	-17%	-6%	-6%	1%	-20%	-20%	9%	11%	-16%	-0%
	3.0kg/h	-11%	-10%	-7%	-11%	-5%	-6%	-10%	-10%	6%	8%	-5%	-1%
	3.5kg/h	-13%	-13%	5%	-13%	-5%	-9%	1%	1%	5%	3%	7%	-8%
	4.0kg/h	7%	6%	31%	7%	10%	9%	27%	27%	20%	20%	41%	-6%
3%	2.0kg/h	13%	12%	-19%	14%	6%	3%	-13%	-17%	11%	9%	-18%	2%
	2.5kg/h	5%	4%	-9%	6%	5%	-3%	-5%	-8%	7%	8%	-8%	4%
	3.0kg/h	-3%	-4%	-4%	-3%	-0%	-11%	-1%	-4%	-1%	1%	-3%	-0%
	3.5kg/h	-5%	-6%	7%	-4%	-3%	-11%	9%	6%	-3%	-4%	8%	-4%
	4.0kg/h	12%	11%	30%	12%	8%	7%	31%	29%	11%	11%	20%	-0%
4%	2.0kg/h	8%	7%	-23%	8%	8%	1%	-20%	-20%	2%	-0%	-22%	-3%
	2.5kg/h	0%	-0%	-15%	0%	4%	-5%	-13%	-13%	-4%	-3%	-15%	-2%
	3.0kg/h	-6%	-6%	-8%	-6%	-2%	-10%	-7%	-6%	-11%	-9%	-8%	-4%
	3.5kg/h	-6%	-6%	4%	-6%	-6%	-9%	5%	5%	-13%	-14%	4%	-4%
	4.0kg/h	11%	11%	27%	11%	3%	9%	27%	27%	2%	2%	21%	4%
5%	2.0kg/h	-1%	-0%	-30%	-1%	7%	7%	-31%	-26%	-8%	-10%	-30%	-7%
	2.5kg/h	-8%	-7%	-23%	-8%	1%	0%	-24%	-19%	-16%	-15%	-23%	-6%
	3.0kg/h	-7%	-5%	-9%	-7%	-1%	1%	-10%	-6%	-17%	-14%	-9%	-1%
	3.5kg/h	-7%	-5%	1%	-7%	-8%	1%	0%	4%	-20%	-22%	1%	2%
	4.0kg/h	-3%	-1%	13%	-3%	-15%	4%	12%	15%	-21%	-20%	8%	2%

Color scale: 45%, 35%, 25%, 15%, 5%, -5%, -15%, -25%, -35%, -45%
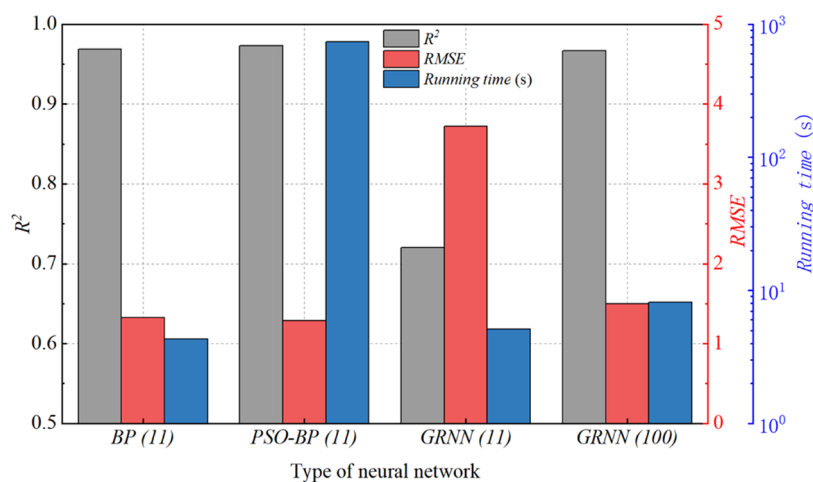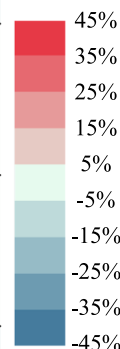
Figure 17. Comparison between BP neural network and PSO-BP neural network, GRNN.

where σ is the surface tension of fuel; ρ_a and ρ_f are air and fuel densities, respectively; μ_a and μ_f are the air and fuel viscosities, respectively; u_a and u_f are the mean velocities of air and fuel at the swirler exit, respectively; ALR is the air-to-fuel ratio (m_a/m_f); and d_0 is a characteristic dimension, which is the diameter of the swirler exit. A, B, and C are empirical constants that depend on the shape of the nozzle and are calculated with the experimental SMD results. Since some correlations contain two unknowns A and B, it is necessary to obtain the optimal solution that satisfies both. In this study, the empirical constants A and B are obtained by two variable linear regression analyses and C is calculated by linear regression analyses.

Lefevre proposed the most widely used correlation 15 for airblast atomization, and this correlation was composed of two parts. The first part considered the effects of aerodynamic force, and the second part considered the physical properties of the liquid. Based on correlation 15, correlations 16−20 were derived by other researchers, which were also widely used for

SMD prediction in the case of airblast atomization. The structures of these correlations were quite similar, with only the exponents modified, or characteristic dimension d_0 was eliminated.

Correlation 21 was derived by Hsiang and Faeth, they focused on the secondary breakup of the droplet and ligaments in the shear breakup regime.

Correlation 22 was developed by Sattlemayer and Wittig based on the experiments with a planar prefilmer; in this correlation, only air velocity and fuel surface tension had effects on droplet size.

Correlation 23 was developed by Aigner and Wittig on the swirl injector; in their opinions, fuel volume and viscosity have no direct effect on droplet size near the prefilmer tip.

More recent formulas for SMD estimation of airblast atomization are correlations 24 and 25.

Correlation 24 was based on the investigation by Chen et al. for air-assisted atomizers. They formulated the correlation with

fuel viscosity, injection pressure, and airblast pressure by using the linear fitting of the design of the experiment (DoE).

Varga et al.'s correlation 23 was based on airblast atomization with a high-velocity gas stream and focused primarily on the disintegration of the liquid jet rather than the droplet sizes.

To evaluate the prediction accuracy quantitatively, the predicted relative errors are summarized in Table 6. The shade of color in the table represented the size of the error. A darker color means a larger error. As can be seen from Table 6, the prediction accuracy of correlations 15, 16, and 18−20 was relatively good, with overall errors within 20%; however, the prediction accuracy of correlations 17, 21, 22, and 25 was very poor, and the prediction error of some conditions reaches more than 40%. The accuracy of BP prediction was within 10%, and the maximum prediction error was only 7%, which was much better than other correlations.

3.4. Comparison between BP Neural Network and Other Neural Networks. As mentioned in the Introduction section, in addition to a BP neural network, there are several neural network models for predicting SMD including particle swarm optimization BP neural network (PSO-BP) and generalized regression neural network (GRNN). PSO algorithm is an evolutionary algorithm developed by Eberhart and Kennedy in 1995.[44] PSO-BP is a BP neural network that uses the PSO algorithm to iteratively optimize the coefficients of each layer in the BP neural network to obtain the best performance.[45] GRNN is a memory-based feed-forward network that is based on the assessment of probability density function.[46] The main function of the GRNN is to estimate a regression surface, whether it is linear or nonlinear, based on the independent variables (also known as input vectors), while considering the dependent variable.[47]

Figure 17 shows the R^2, RMSE, and running time of the BP neural network, PSO-BP, and GRNN. It can be found that the R^2 and RMSE performances of BP and PSO-BP are similar, but the running time of PSO-BP is much longer than that of the BP neural network. The R^2 and RMSE of GRNN are worse than those of the BP neural network under the same number of hidden layers (11 layers). When the number of hidden layers of the GRNN increases to 100, the prediction results of GRNN and BP are similar. This indicated that, for the predicting target in the present study, the BP neural network shows the advantages of simple structure and short running time compared with other neural networks.

4. CONCLUSIONS

The purpose of this study was to establish a novel and effective SMD prediction model for a swirl cup airblast fuel injector by the BP neural network. Geometry parameters (primary swirl number, secondary swirl number, venturi angle), condition parameters (mass flow rate of fuel, relative air pressure drop), and axial distance from the swirler exit were used to train the BP neural network model.

The results show that a BP neural network model can be successfully developed for a highly accurate SMD prediction with smaller RMSE and higher R^2. Through validation by extra experimental SMD results, it is implied that the BP neural network model has good generalization and is able to predict other swirl cup airblast fuel injector geometric combinations.

Based on sensitivity analysis of input parameters in the BP neural network model, it could be obtained that the relative air pressure drop and primary swirl number were the largest and smallest factors affecting the SMD prediction accuracy. For the swirl cup airblast fuel injector used in this study, geometry parameters had a greater influence on SMD than the condition parameters.

In addition, compared with the empirical and semiempirical correlations of SMD in previous studies, the BP neural network model shows lower prediction error, which is superior to those correlations in previous studies. Moreover, for the predicting target in the present study, the BP neural network shows the advantages of a simple structure and short running time compared with PSO-BP and GRNN.

Hence, the BP neural network model is more suitable for the SMD prediction for the complex atomization process of the swirl cup airblast fuel injector.

■ AUTHOR INFORMATION

Corresponding Authors

Shaolin Wang − *Laboratory of Light-Duty Gas-Turbine, Institute of Engineering Thermophysics, Chinese Academy of Sciences, Beijing 100190, China; University of Chinese Academy of Sciences, Beijing 100049, China; Innovation Academy for Light-duty Gas Turbine, Beijing 100190, China*; Email: wangshaolin@iet.cn

Cunxi Liu − *Laboratory of Light-Duty Gas-Turbine, Institute of Engineering Thermophysics, Chinese Academy of Sciences, Beijing 100190, China; University of Chinese Academy of Sciences, Beijing 100049, China; Innovation Academy for Light-duty Gas Turbine, Beijing 100190, China;* orcid.org/0000-0002-7757-1632; Email: liucunxi@iet.cn

Authors

Chuanyu Fang − *Laboratory of Light-Duty Gas-Turbine, Institute of Engineering Thermophysics, Chinese Academy of Sciences, Beijing 100190, China; University of Chinese Academy of Sciences, Beijing 100049, China; Innovation Academy for Light-duty Gas Turbine, Beijing 100190, China;* orcid.org/0009-0001-6176-0340

Fuqiang Liu − *Qingdao Institute of Aeronautical Technology, Qingdao 266400 Shandong, China*

Jinhu Yang − *Qingdao Institute of Aeronautical Technology, Qingdao 266400 Shandong, China*

Yong Mu − *Qingdao Institute of Aeronautical Technology, Qingdao 266400 Shandong, China*

Gang Xu − *Laboratory of Light-Duty Gas-Turbine, Institute of Engineering Thermophysics, Chinese Academy of Sciences, Beijing 100190, China; University of Chinese Academy of Sciences, Beijing 100049, China; Innovation Academy for Light-duty Gas Turbine, Beijing 100190, China*

Junqiang Zhu − *Laboratory of Light-Duty Gas-Turbine, Institute of Engineering Thermophysics, Chinese Academy of Sciences, Beijing 100190, China; University of Chinese Academy of Sciences, Beijing 100049, China; Innovation Academy for Light-duty Gas Turbine, Beijing 100190, China*

Yushuai Liu − *Laboratory of Light-Duty Gas-Turbine, Institute of Engineering Thermophysics, Chinese Academy of Sciences, Beijing 100190, China; University of Chinese Academy of Sciences, Beijing 100049, China; Innovation Academy for Light-duty Gas Turbine, Beijing 100190, China*

Complete contact information is available at:
https://pubs.acs.org/10.1021/acsomega.3c03232

Notes

The authors declare no competing financial interest.

■ NOMENCLATURE

ALR	air-to-liquid mass flow ratio
A, B, C	experimental parameters, varying dimensions
b	bias
d_0	characteristic size, mm
G_φ	axial flux of the angular momentum
G_z	axial thrust
I, O	the number of neurons in the input and output layer
P	pressure, MPa
SD	standard deviation.
RMSE	root mean square error
R^2	coefficient of determination
SN	Swirl number
SMD	Sauter mean diameter
u	velocity, m/s
wd	axial width of primary swirl channel
w	weight
Z	axial positions from fuel injector exit

■ GREEK CHARACTERS

α	primary swirler angle
β	secondary swirler angle
θ	angle
ψ	blockage factor
Δ	differential between the inlet and exit
ρ	density, kg/m3
σ	surface tension, N/m
μ	dynamic viscosity, kg/(m·s)

■ ABBREVIATIONS

PDPA	phase doppler particle analyzer
BP	backpropagation neural network
ANN	artificial neural network

■ SUBSCRIPTS

a	air
f	fuel
r	radial distance of measurement points from the swirler cup axis
p	primary swirl
s	secondary swirl
v	venturi
i, j, k	BP neural network nodes
M	measured value
P	prediction value

■ REFERENCES

(1) Lefebvre, A. H. Airblast atomization. *Prog. Energy Combust. Sci.* **1980**, *6* (3), 233−261.

(2) Fu, Y.; Cai, J.; Jeng, S. M.; Mongia, H. In *Confinement Effects on the Swirling Flow of a Counter-Rotating Swirl Cup, Asme Turbo Expo: Power for Land, Sea, & Air*, 2005; pp 469−478.

(3) Lin, S.-C.; Wang, X.; Estefanos, W.; Tambe, S.; Jeng, S.-M. *The Effect of the Geometric Modifications of the Venturi on the Non-Reactive Flow and Combustion Behavior Using a Counter-Rotating Radial-Radial Swirler, ASME Turbo Expo 2017: Turbomachinery Technical Conference and Exposition*, 2017.

(4) Liu, C.; Liu, F.; Yang, J.; Mu, Y.; Hu, C.; Xu, G. Experimental Investigation of Spray and Combustion Performances of a Fuel-Staged Low Emission Combustor: Effects of Main Swirl Angle. *J. Eng. Gas Turbines Power* **2017**, *139* (12), GTP-16-1329 DOI: 10.1115/1.4037451.

(5) Wang, H. Y.; McDonell, V. G.; Samuelsen, S. *Influence of Hardware Design on the Flow Field Structures and the Patterns of Droplet Dispersion: Part I — Mean Quantities, ASME 1993 International Gas Turbine and Aeroengine Congress and Exposition*, 1993.

(6) Becker, J.; Hassa, C. *Experimental Investigation of Spatial and Temporal Aspects of the Liquid Fuel Placement in a Swirl Cup at Elevated Pressure, ASME Turbo Expo 2004: Power for Land, Sea, and Air*, 2004, pp 351−360.

(7) Shanmugadas, K. P.; Manuprasad, E. S.; Chiranthan, R. N.; Chakravarthy, S. R. Fuel placement and atomization inside a gas-turbine fuel injector at realistic operating conditions. *Proc. Combust. Inst.* **2021**, *38* (2), 3261−3268.

(8) Huang, Y.; Yang, V. Dynamics and stability of lean-premixed swirl-stabilized combustion. *Prog. Energy Combust. Sci.* **2009**, *35* (4), 293−364.

(9) Im, K.-S.; Kim, H.; Lai, M.-C.; Tacina, R. Parametric Study of the Swirler/Venturi Spray Injectors. *J. Propul. Power* **2001**, *17* (3), 717−727.

(10) Ateshkadi, A.; McDonell, V.; Samuelsen, G. *Effect of Mixer Geometry on Fuel Spray Distribution, Emissions and Stability*, 36th AIAA Aerospace Sciences Meeting and Exhibit, 1998.

(11) Liu, C.; Liu, F.; Yang, J.; Mu, Y.; Xu, G. Investigations of the effects of spray characteristics on the flame pattern and combustion stability of a swirl-cup combustor. *Fuel* **2015**, *139*, 529−536.

(12) Lefebvre, A. H. Airblast atomization. *Prog. Energy Combust. Sci.* **1980**, *6* (3), 233−261.

(13) Hashimoto, N.; Nishida, H.; Ozawa, Y. Fundamental combustion characteristics of Jatropha oil as alternative fuel for gas turbines. *Fuel* **2014**, *126*, 194−201.

(14) Jasuja, A. K. Atomization of Crude and Residual Fuel Oils. *J. Eng. Power* **1979**, *101* (2), 250−258.

(15) Urbán, A.; Zaremba, M.; Malý, M.; Józsa, V.; Jedelský, J. Droplet dynamics and size characterization of high-velocity airblast atomization. *Int. J. Multiphase Flow* **2017**, *95*, 1−11.

(16) Chong, C. T.; Hochgreb, S. Effect of Atomizing Air Flow on Spray Atomization of an Internal-mix Twin-fluid Atomizer. *Atomization Sprays* **2015**, *25* (8), 657−673.

(17) Yang, F.; Cho, H.; Zhang, H.; Zhang, J.; Wu, Y. Artificial neural network (ANN) based prediction and optimization of an organic Rankine cycle (ORC) for diesel engine waste heat recovery. *Energy Convers. Manage.* **2018**, *164*, 15−26.

(18) Cui, Y.; Liu, H.; Wang, Q.; Zheng, Z.; Wang, H.; Yue, Z.; Ming, Z.; Wen, M.; Feng, L.; Yao, M. Investigation on the ignition delay prediction model of multi-component surrogates based on back propagation (BP) neural network. *Combust. Flame* **2022**, *237*, 111852 DOI: 10.1016/j.combustflame.2021.111852.

(19) Zhao, F.; Ruan, Z.; Yue, Z.; Hung, D. L. S.; Som, S.; Xu, M. Time-sequenced flow field prediction in an optical spark-ignition direct-injection engine using bidirectional recurrent neural network (bi-RNN) with long short-term memory. *Appl. Therm. Eng.* **2020**, *173*, 115253 DOI: 10.1016/j.applthermaleng.2020.115253.

(20) Kaiser, R.; Kim, S.; Lee, D. Deep data analysis for aspiration pressure estimation in a high-pressure gas atomization process using an artificial neural network. *Chem. Eng. Process.* **2020**, *153*, 107924 DOI: 10.1016/j.cep.2020.107924.

(21) Park, Y.; Choi, M.; Kim, K.; Li, X.; Jung, C.; Na, S.; Choi, G. Prediction of operating characteristics for industrial gas turbine combustor using an optimized artificial neural network. *Energy* **2020**, *213*, 118769 DOI: 10.1016/j.energy.2020.118769.

(22) Taghavifar, H.; Khalilarya, S.; Jafarmadar, S. Diesel engine spray characteristics prediction with hybridized artificial neural network optimized by genetic algorithm. *Energy* **2014**, *71*, 656−664.

(23) Ghorbanian, K.; Soltani, M. R.; Morad, M. R.; Ashjaee, M. In *Neural Network Prediction of a Liquid-Liquid Coaxial Swirl Injector Performance Map*, 43rd AIAA Aerospace Sciences Meeting and Exhibit, 2005.

(24) Liu, C.; He, L. Atomized droplet size prediction for supersonic atomized water drainage and natural gas extraction. *Sci. Rep.* **2022**, *12* (1), No. 22192.

(25) Chigier, N. A.; Bee′r, J. M. Velocity and Static-Pressure Distributions in Swirling Air Jets Issuing From Annular and Divergent Nozzles. *J. Basic Eng.* **1964**, *86* (4), 788−796.

(26) Sheen, H. J.; Chen, W. J.; Jeng, S. Y.; Huang, T. L. Correlation of swirl number for a radial-type swirl generator. *Exp. Therm. Fluid Sci.* **1996**, *12* (4), 444−451.

(27) Ma, H.; Xie, M.; Zeng, W.; Chen, B. Experimental study on combustion characteristics of Chinese RP-3 kerosene. *Chin. J. Aeronaut.* **2016**, *29* (2), 375−385.

(28) Shin, D.; Satija, A.; Lucht, R. P. Spray characteristics of standard and alternative aviation fuels at high ambient pressure conditions. *Exp. Therm. Fluid Sci.* **2022**, *130*, 110511 DOI: 10.1016/j.expthermflusci.2021.110511.

(29) Liu, G.; Jia, L.; Kong, B.; Feng, S.; Zhang, H.; Zhang, H. Artificial neural network application to microstructure design of Nb-Si alloy to improve ultimate tensile strength. *Mater. Sci., Eng.: A* **2017**, *707*, 452−458.

(30) Feng, Y.-q.; Liu, Y.-Z.; Wang, X.; He, Z.-X.; Hung, T.-C.; Wang, Q.; Xi, H. Performance prediction and optimization of an organic Rankine cycle (ORC) for waste heat recovery using back propagation neural network. *Energy Convers. Manage.* **2020**, *226*, No. 113552.

(31) Al-Wahaibi, T.; Mjalli, F. S. Prediction of Horizontal Oil-water Flow Pressure Gradient Using Artificial Intelligence Techniques. *Chem. Eng. Commun.* **2014**, *201* (2), 209−224.

(32) Varol, T.; Canakci, A.; Ozsahin, S. Artificial neural network modeling to effect of reinforcement properties on the physical and mechanical properties of Al2024−B4C composites produced by powder metallurgy. *Composites, Part B* **2013**, *54*, 224−233.

(33) Mohanty, Y. K.; Mohanty, B. P.; Roy, G. K.; Biswal, K. C. Effect of secondary fluidizing medium on hydrodynamics of gas−solid fluidized bed—Statistical and ANN approaches. *Chem. Eng. J.* **2009**, *148* (1), 41−49.

(34) Hornik, K.; Stinchcombe, M.; White, H. Multilayer feedforward networks are universal approximators. *Neural Networks* **1989**, *2* (5), 359−366.

(35) Ma, X.; Guan, Y.; Mao, R.; Zheng, S.; Wei, Q. Modeling of lead removal by living Scenedesmus obliquus using backpropagation (BP) neural network algorithm. *Environ. Technol. Innovation* **2021**, *22*, No. 101410.

(36) Lek, S.; Belaud, A.; Baran, P.; Dimopoulos, I.; Delacoste, M. J. A. L. R. Role of some environmental variables in trout abundance models using neural networks. *Aquat. Living Resour.* **1996**, *9* (1), 23−29.

(37) El-Shanawany, M. S.; Lefebvre, A. H. Airblast Atomization: Effect of Linear Scale on Mean Drop Size. *J. Energy* **1980**, *4* (4), 184−189.

(38) Rizk, N. K.; Lefebvre, A. H. In *Spray Characteristics of Plain-Jet Airblast Atomizers*, ASME 1983 International Gas Turbine Conference and Exhibit, 1983.

(39) Hsiang, L. P.; Faeth, G. M. Near-limit drop deformation and secondary breakup. *Int. J. Multiphase Flow* **1992**, *18* (5), 635−652.

(40) Sattelmayer, T.; Wittig, S. Internal Flow Effects in Prefilming Airblast Atomizers: Mechanisms of Atomization and Droplet Spectra. *J. Eng. Gas Turbines Power* **1986**, *108* (3), 465−472.

(41) Aigner, M.; Wittig, S. Swirl and Counterswirl Effects in Prefilming Airblast Atomizers. *J. Eng. Gas Turbines Power* **1988**, *110* (1), 105−110.

(42) Chen, L.; Liu, Z.; Sun, P.; Huo, W. Formulation of a fuel spray SMD model at atmospheric pressure using Design of Experiments (DoE). *Fuel* **2015**, *153*, 355−360.

(43) Varga, C. M.; Lasheras, J. C.; Hopfinger, E. J. Initial breakup of a small-diameter liquid jet by a high-speed gas stream. *J. Fluid Mech.* **2003**, *497*, 405−434.

(44) Kennedy, J.; Eberhart, R. In *Particle swarm optimization, 1995 IEEE International Conference on Neural Networks (ICNN 95)*, Univ W Australia, Perth, Australia, 1995 Nov 27−Dec 01; pp 1942−1948.

(45) Ren, C.; An, N.; Wang, J. Z.; Li, L.; Hu, B.; Shang, D. Optimal parameters selection for BP neural network based on particle swarm optimization: A case study of wind speed forecasting. *Knowledge-Based Syst.* **2014**, *56*, 226−239.

(46) Specht, D. F. A General Regression Neural Network. *IEEE Trans. Neural Networks* **1991**, *2* (6), 568−576.

(47) Li, H.-z.; Guo, S.; Li, C.-j.; Sun, J.-q. A hybrid annual power load forecasting model based on generalized regression neural network with fruit fly optimization algorithm. *Knowledge-Based Systems* **2013**, *37*, 378−387.